

# Hybrid FEM-NN models: Combining artificial neural networks with the finite element method

Sebastian K. Mitusch<sup>a,\*</sup>, Simon W. Funke<sup>a</sup>, Miroslav Kuchta<sup>a</sup>

<sup>a</sup>*Simula Research Laboratory, 1364 Fornebu, Norway*

---

## Abstract

We present a methodology combining neural networks with physical principle constraints in the form of partial differential equations (PDEs). The approach allows to train neural networks while respecting the PDEs as a strong constraint in the optimisation as apposed to making them part of the loss function. The resulting models are discretised in space by the finite element method (FEM). The methodology applies to both stationary and transient as well as linear/nonlinear PDEs. We describe how the methodology can be implemented as an extension of the existing FEM framework FEniCS and its algorithmic differentiation tool dolfin-adjoint. Through series of examples we demonstrate capabilities of the approach to recover coefficients and missing PDE operators from observations. Further, the proposed method is compared with alternative methodologies, namely, physics informed neural networks and standard PDE-constrained optimisation. Finally, we demonstrate the method on a complex cardiac cell model problem using deep neural networks.

**Keywords:** Data-driven scientific computing, Partial differential equations, Learning unknown physics, Machine learning, Finite element method

---

## 1. Introduction

The plummeting cost of physical sensors, computational power, and data storage results in an explosion of data, and the task of manually extracting information from that data has become overwhelming. In the last decade, statistical learning, and specifically artificial neural networks (NN), have proven to be immensely valuable in meeting these challenges. One disadvantage of neural networks is however that a priori they embed no inherent knowledge of the physical, or mathematical, laws governing the underlying systems at hand [1]. Embedding such knowledge is non trivial, requiring e.g. novel architectures [2, 3, 4] or problem formulations [5].

Conversely, models based on physical principles, typically described by partial differential equations

---

\*Corresponding author

*Email addresses:* `sebastian@simula.no` (Sebastian K. Mitusch), `simon@simula.no` (Simon W. Funke), `miroslav@simula.no` (Miroslav Kuchta)

(PDEs), have been employed for centuries; these models have the advantages of a solid mathematical foundation and a wide array of numerical methods facilitating their solution. Such models also have their disadvantages; constructing PDE models, and pursuant solution techniques, is an arduous task. PDE models are often rigid, relying on explicit assumptions, or are so large as to be computationally infeasible. The primary limitation of PDE models is a lack of ability to learn new principles from observational input.

Bridging the gap between explicit PDE systems and observation-driven NN learning to overcome the limitations of either approaches has recently gained scientific traction. Raissi et al. [5] introduced physics-informed neural networks (PINNs) for solving PDEs by training a neural network with a loss function consisting of the PDE residual. They further demonstrate that PINNs can be combined with discovery of governing equations through identification of coefficients in the PDE. This equation discovery technique was later demonstrated with a neural network approximator [6, 7]. PINNs are able to approximate solutions even of complex non-linear PDEs, which is essential when using a neural network approximator for equation discovery.

However, when combining equation discovery with PINNs the training problem becomes more complex. Instead of only training to find an approximation for the unknown equation terms, the training process also involves approximating the solution to this equation. This additional training step might be unnecessary if traditional solvers for PDEs are used to solve the approximated equation. Furthermore, traditional PDE solvers such as the finite element method (FEM) or finite volume method have rich theory, providing convergence guarantees. In comparison, such theories for PINNs have only recently emerged [8].

In this paper, we propose a methodology to combine the finite element method with neural networks. The aim is to obtain an approach that combines the strengths of PDE-based modelling, e.g. the geometric flexibility and rich set of finite element functions of the finite element method, with the flexibility of neural networks to express unknown functions. Equation discovery using traditional PDE solvers in conjunction with neural networks has previously been demonstrated [9, 10, 11, 12]. In [9] a neural network with a single hidden layer is used to approximate a spatially varying diffusion coefficient in the Poisson equation that was discretised with the finite element method. The authors demonstrate that neural networks provide an implicit regularisation, achieving smoother solutions than finite element functions with no explicit regularisation. The framework ADCME.jl presented in [11] enables training of finite element models with neural networks. While the framework has been demonstrated on learning constitutive relations and physical parameters in the steady state Navier-Stokes equation [11, 12], it (currently) lacks support for time-dependent problems. Rackauckas et. al [10] propose Universal Differential Equations in which ODEs and PDEs are augmented with neural networks on finite difference schemes. The results show promise for the development of hybrid PDE-NN models, but do not demonstrate the combination of more flexible PDE discretisation methods such as the FEM.

Here we present a novel approach for training neural networks augmenting PDEs, which addresses some of the shortcomings of the previous works. In particular, the approach applies to both stationary and transient as well as linear/non-linear PDEs. The hybrid PDE-NN models are discretised in space using FEM, enabling the use of the well-established finite element framework FEniCS [13]. The neural networks can either be defined directly in FEniCS or through the machine learning library PyTorch [14]. We demonstrate the approach on a variety of problems, including problems with partial observations, noisy observations and deep neural networks. Our work is structured as follows. In section 2 the hybrid FEM-NN methodology is introduced in a general setting along with details about discretisation and the resulting optimisation problem. Afterwards, section 3 presents a range of examples of increasing complexity. Finally, section 4 summarizes and provides discussion on future work.

## 2. Framework for hybrid FEM-NN models

In the most general sense, we consider hybrid models of form

$$E(u, \mathcal{N}(\cdot; W)) = 0 \quad \text{in } \Sigma \quad (1)$$

Here,  $\Sigma$  is typically a spatio-temporal domain  $\Sigma = \Omega \times (0, T)$  and  $E$  is a differential operator that defines the PDE augmented with neural networks. For example,  $E$  can be defined as  $\frac{\partial u}{\partial t} - \nabla \cdot \mathcal{N}(\cdot; W) \nabla u - f$  describing the heat equation with source term  $f$  and solution  $u$ , with an approximate heat diffusion coefficient  $\mathcal{N}$  given by neural network with weights  $W$ .

Commonly when the physics is only partially known, the unknown physical component can be more easily formulated in an additive way. Additionally, we mainly focus on time-dependent problems, from which we can formulate a specific class of hybrid PDE-NN models

$$\begin{aligned} u_t &= F(u) + \mathcal{N}(u; W) && \text{in } \Omega \times (0, T), \\ u &= u_0 && \text{on } \Omega \times \{t = 0\} \end{aligned} \quad (2)$$

with solution  $u : \Omega \times (0, T) \rightarrow \mathbb{R}^d$  defined on the space-time cylinder  $\Omega \times (0, T)$  and  $\Omega \subset \mathbb{R}^n$ . Here,  $F(u) : \Omega \times (0, T) \rightarrow \mathbb{R}^d$  represents an ordinary or partial differential operator, and  $\mathcal{N}(u; W) : \Omega \times (0, T) \rightarrow \mathbb{R}^d$  an artificial neural network with weights  $W$ <sup>1</sup>. In addition, suitable boundary conditions must be added to eq. (2) to close the system.

We remark that eq. (2) can be considered as a generalization of two limit cases. If  $\mathcal{N} \equiv 0$ , then the problem reduces to a traditional differential equation. Similarly, if  $F \equiv 0$  one obtains a continuous in time residual neural network, which if discretised with an explicit Euler scheme, reduces to a standard residual neural network [15, 16].

---

<sup>1</sup>For simplicity, we assume that the neural networks only use point evaluations of the solution  $u$ . In other words, the neural network takes the form  $\mathcal{N}(u; W)(x) = \mathcal{N}(W)(x, u(x), u_x(x), \dots)$ .

### 2.1. Discretisation in time

We consider two strategies for discretising eq. (2) in time: a direct discretisation and operator splitting. Using for instance a  $\theta$ -method in the first approach yields for each timestep a problem

$$u^{n+1} - u^n = \Delta t (F(u^{n+\theta}) + \mathcal{N}(u^{n+\theta}; W)) \quad \text{in } \Omega, \quad (3)$$

where  $\Delta t$  denotes the time step and  $u^{n+\theta} := (1 - \theta)u^n + \theta u^{n+1}$ . Depending on the choice of  $\theta$  one obtains an explicit Euler ( $\theta = 0$ ), semi-implicit Crank-Nicolson ( $\theta = 1/2$ ) or implicit Euler ( $\theta = 1$ ) method. This approach has some difficulties in practice. The first challenge is to solve the highly non-linear problem eq. (3) that arises at each time-step for  $\theta > 0$ . The non-linearity stems primarily from the activation functions in the neural network  $\mathcal{N}$  and will increase with the complexity of the neural network architecture. As a result, the convergence radius of standard non-linear solvers such as Newton's method, can be very small and might force the usage of very small time-steps or advanced non-linear solvers. The second difficulty is to solve the linear subproblems that arise during each non-linear iteration. The dimension of these linear problems is typically large and tailored preconditioners for iterative linear solvers are required to solve them efficiently. However, the left hand side of the linear problem contains both a linearised PDE operator and a linearised neural network. Preconditioners for such linear problems have not been developed yet. We apply the direct approach eq. (3) to examples presented further in sections 3.2 and 3.3.

In the operator splitting approach eq. (2) is decomposed into simpler problems that can be treated individually using specialized numerical algorithms. For instance, applying the Marchuk-Yanenko [17] splitting to eq. (2) yields two subproblems for each timestep:

$$\begin{aligned} \bar{u}^{n+1} &= u^n + \Delta t F(\bar{u}^{n+\theta}) && \text{in } \Omega, \\ u^{n+1} &= \bar{u}^{n+1} + \Delta t \mathcal{N}(\bar{u}^{n+1}; W) && \text{in } \Omega \end{aligned} \quad (4)$$

with  $\bar{u}^{n+\theta} = \theta \bar{u}^{n+1} + (1 - \theta)u^n$ ,  $0 \leq \theta \leq 1$ . Note that the first subproblem corresponds to a pure PDE problem, while the second subproblem reduces to a residual neural network step. We remark that the Marchuk-Yanenko splitting scheme is only first order accurate. Thus, it can be preferable to use Strang [17] splitting which is formally second-order accurate for sufficiently smooth operators  $F$  and  $\mathcal{N}$ .

The operator splitting approach overcomes most of the difficulties that arise with the first strategy. Firstly, the PDE and neural network operators are different in nature and hence require different numerical solution techniques. For instance, a natural choice is to treat the PDE subproblems implicitly, and the NN subproblem explicitly, potentially even with substepping. Secondly, splitting enables the usage of specialised numerical methods to each subproblem. This is particularly important for the first subproblem, for which there exist well-established discretisation schemes, such as the finite element method, as well as fast iterative solvers and preconditioners. In addition, the splitting approach allows us to use two specialized software

frameworks of highly efficient and well-tested numerical methods, e.g. FEniCS [13] for the PDE part and PyTorch [14] for the NN part. The splitting approach eq. (4) is applied to the problem studied in section 3.4.

## 2.2. Discretisation in space

We employ the finite element method for the spatial discretisation of the hybrid PDE-NN problems eq. (3) and eq. (4). Let  $\Omega_h$  be a triangulation of the domain  $\Omega$  with  $h > 0$  a characteristic size of the elements and let  $U, V$  be suitable, discrete finite element spaces of trial and test functions. Then, the variational form of eq. (3) reads: Find  $u^{n+1} \in U$  such that for all  $v \in V$

$$\int_{\Omega} (u^{n+1} - u^n) \cdot v dx = \Delta t \int_{\Omega} F(u^{n+\theta}) \cdot v dx + \Delta t \int_{\Omega} \mathcal{N}(u^{n+\theta}) \cdot v dx. \quad (5)$$

We remark that the finite element spaces and functions depend on the mesh size parameter, however, for simplicity of notation we do not write  $u_h, v_h$  or  $U_h, V_h$  and only use the subscript when the dependence needs to be highlighted.

For the Marchuk-Yanenko splitting scheme eq. (4), the variational problem become: First, find  $\bar{u}^{n+1} \in U$  such that

$$\int_{\Omega} (\bar{u}^{n+1} - u^n) \cdot v dx = \Delta t \int_{\Omega} F(\bar{u}^{n+\theta}) \cdot v dx \quad (6)$$

for all  $v \in V$ . Then, find  $u^{n+1} \in U$  such that

$$\int_{\Omega} (u^{n+1} - \bar{u}^{n+1}) \cdot v dx = \Delta t \int_{\Omega} \mathcal{N}(\bar{u}^{n+1}) \cdot v dx \quad (7)$$

for all  $v \in V$ . If  $\mathcal{N}(\bar{u}^n) \in U$  the second problem can be solved pointwise as

$$u^{n+1}(x) = \bar{u}^{n+1}(x) + \Delta t \mathcal{N}(\bar{u}^n)(x). \quad (8)$$

Note that both eq. (5) and eq. (7) require integration of a neural network over the spatial domain  $\Omega$ . This can be a major challenge as there is currently no theory on optimal quadrature rules for NNs, and deriving the analytical expression for these integrals is practically infeasible as the network grows [18]. Thus, in order to compute these integrals we use a Gaussian quadrature rule (on the triangulation  $\Omega_h$ ) with a degree based on the discretisation scheme used.

## 2.3. Training procedure and adjoint equation

While in regular NN problems one often has direct data on the NN output, in our methodology the direct NN output is assumed unknown and only data on what the solution of the PDE-NN model should match are provided. Thus, the cost function to be minimised measures the error of the NN output only indirectly through the solution of the PDE-NN model.

Let  $\mathcal{U} = \{u_i + \epsilon_i\}_{i=1}^n$  be the set of  $n$  training observations, where  $\epsilon_i$  is some potential Gaussian noise  $\epsilon_i \sim N(0, \sigma^2)$  for each  $i = 1, 2, \dots, n$ . Further, let  $\hat{u}_i$  denote the solution of the PDE-NN model with the current set of weights  $W$ . Then the cost function is a sum over the loss of each individual observation,  $\sum_{i=1}^n L(\hat{u}_i, u_i)$ , with the loss function  $L$  being problem dependent. For example,  $L$  could be defined as the  $L^2(\Omega)$  error at an observation time point.

Having defined the loss, the minimisation/learning problem of the PDE-NN approach is now

$$\min_{W, \hat{u}_1, \hat{u}_2, \dots, \hat{u}_n} \sum_{i=1}^n L(\hat{u}_i, u_i) \text{ subject to } \hat{u}_t = F(\hat{u}) + N(\hat{u}; W) \quad (9)$$

and we observe that eq. (9) is a *constrained* optimisation problem. Traditionally, neural networks are trained using back-propagation, which involves computing the gradient of the cost using reverse mode algorithmic differentiation (AD). In reverse mode AD the gradient is computed by the adjoint of an expansion through the chain rule [19], which in our problem setting would consist of computing  $\frac{\partial \hat{u}_i}{\partial W}^* [s]$ . Here  $s$  is the result of previous gradient computations, typically  $s = \frac{dL}{du}$  and  $*$  denotes the Hermitian adjoint. Under some assumptions, this adjoint operator can be efficiently computed using the adjoint equation. Efficiently in that the computational cost does not scale multiplicatively with the number of weights in the neural network.

Let us assume that the operator  $E(\hat{u}, W) = \hat{u}_t - F(\hat{u}) + N(\hat{u}; W)$  is continuously differentiable, with a unique solution  $\hat{u}$  for each configuration of weights  $W$ . Thus, there is a solution operator  $\hat{u}(W)$  such that  $E(\hat{u}(W), W) = 0$ . Further assuming that the linearised operator  $\partial E(\hat{u}(W), W)/\partial \hat{u}$  is continuously invertible, by the implicit function theorem, the solution operator  $\hat{u}(W)$  is continuously differentiable and its derivative is given through the following equation [20]

$$\frac{\partial E(\hat{u}(W), W)}{\partial \hat{u}} \frac{\partial \hat{u}(W)}{\partial W} + \frac{\partial E(\hat{u}(W), W)}{\partial W} = 0.$$

It follows that the adjoint operator  $\frac{\partial \hat{u}_i}{\partial W}^* [s]$  is given by

$$\frac{\partial \hat{u}_i}{\partial W}^* [s] = - \frac{\partial E(\hat{u}(W), W)}{\partial W}^* \frac{\partial E(\hat{u}(W), W)}{\partial \hat{u}}^{-*} [s].$$

Introducing an auxiliary variable named the adjoint state  $\lambda$ , the gradients for the PDE solution are computed in two steps: First by solving the adjoint equation

$$\frac{\partial E(\hat{u}(W), W)}{\partial \hat{u}}^* \lambda_s = s.$$

Second by using the acquired adjoint state to compute the gradient contributions from the PDE solution

$$\frac{\partial \hat{u}_i}{\partial W}^* [s] = - \frac{\partial E(\hat{u}(W), W)}{\partial W}^* \lambda_s.$$

Note that while the equation  $E(\hat{u}(W), W) = 0$  may be nonlinear, the adjoint equation is always linear.

In the case of a nonlinear PDE  $E(\hat{u}(W), W) = 0$  an iterative scheme such as Newton's method or Picard iterations is employed. This solution process involves solving many linearised systems, which (hopefully)

approaches the true solution of the nonlinear PDE. Assuming that the final solution is close to the true solution, the adjoint equation is solved only once for the nonlinear PDE. Thus, backpropagation through a nonlinear PDE will involve as many or fewer linear solves than the forward computations.

With the adjoint method we have a way to efficiently compute gradients of the now *unconstrained* optimisation problem

$$\min_W \sum_{i=1}^n L(\hat{u}_i(W), u_i).$$

From the perspective of the back-propagation algorithm, the PDE solver is just as any other arithmetic operation which we can differentiate. This enables the integration with existing machine learning frameworks such as PyTorch [14].

#### 2.4. Implementation

In order to solve the PDEs with FEM we employ the finite element framework FEniCS [13] which allows PDEs to be specified through the domain specific language UFL [21]. Using UFL the user defines the PDE through its discrete variational formulation with close to mathematical notation. For example, defining the variational formulation of the PDE  $F := -\Delta u - f = 0$  amounts to:

```
F = grad(u)*grad(v)*dx - f*v*dx
```

After defining the variational form, it can be used with the FEniCS interface to automatically assemble and solve the system. Using dolfin-adjoint [22] the PDE solution can be automatically differentiated. Exploiting the symbolic representation of the variational formulation of the PDE, in addition to the symbolic differentiation capabilities of UFL, dolfin-adjoint derives the UFL expression for the adjoint equation and solves it using the same discretisation as the original PDE solver.

The NNs can be defined directly in UFL, allowing the FEniCS backend to take care of the evaluation at integration points. For example, a single hidden layer of a NN  $v_1 = \sigma(W_1x + W_2)$  with weights  $W_1$ , bias  $W_2$ , and activation function  $\sigma = \tanh$  can be expressed in UFL as

```
sigma = ufl.tanh
v_1 = sigma(W_1 * ufl.as_vector([x]) + W_2)
```

However, UFL does not have built-in support for vectorized activation functions. Thus, if the output is not scalar, one has to loop over the output:

```
def sigma(v_0):
    return ufl.as_vector([ufl.tanh(v_0[i]) for i in range(v_0.ufl_shape[0])])
```

In a similar way one can easily build UFL expressions for arbitrary layered feed-forward NNs, using the class ANN in the snippet below. The ANN class can be found at <https://github.com/sebastkm/hybrid-fem-nn>.

In turn, a hybrid PDE-NN training problem can be defined in a few lines of code. For example, the Poisson problem from section 3.1 with an assumed unknown spatially varying source  $f$  term approximated by a NN with 10 hidden neurons and scalar output reads:

```
from fenics import *
from dolfin_adjoint import *

from neural_network import ANN

# Setup mesh, FE space V with boundary conditions 'bcs'
# Let observations be 'obs'
hat_u = Function(V)

layers = [2, 10, 1]
bias = [True, True]
x, y = SpatialCoordinate(mesh)
net = ANN(layers, bias=bias, mesh=mesh)
E = inner(grad(u), grad(v))*dx - net([x, y])*v*dx

# Solve PDE
solve(lhs(E) == rhs(E), hat_u, bcs)

# L^2 error as loss
loss = assemble((hat_u - obs)**2*dx)

# Define reduced formulation of problem
hat_loss = ReducedFunctional(loss, net.weights_ctrls())

# Use scipy L-BFGS optimiser
opt_theta = minimize(hat_loss, method="L-BFGS-B")
```

This pure UFL approach allows for the whole implementation to only rely on FEniCS and dolfin-adjoint. If we instead wish to approximate  $f$  using a NN implemented outside of UFL, for example in PyTorch, we proceed by interpolating the NN to a finite element space. The details of this will be discussed in a future paper.

### 3. Examples

In this section, we present several examples illustrating the capabilities of hybrid PDE-NN models. First, the methodology is demonstrated on a Poisson problem in section 3.1. The goal is to investigate performance of the proposed approach in different scenarios with regards to discretisation and observations. Then, in

section 3.2 the methodology is compared on a simple heat equation problem against a pointwise estimator and a physics-informed neural network approach. In section 3.3 we try to recover a missing advection term in the advection-diffusion equation. Finally, in section 3.4 the method is demonstrated on a challenging problem from the field of cardiac electrophysiology.

For the following examples, we will be looking at equations on the form of eq. (2). For these examples,  $\hat{u}$  will denote the approximate state, while  $u$  denotes the true state on some spatio-temporal domain  $\Omega \times \mathcal{T}$  with  $\mathcal{T} = (0, T)$ . To measure the accuracy of a trained model over the whole domain, we employ the following measures:

$$e_{\Omega \times \mathcal{T}}^2(\hat{u}, u) = \frac{\int_{\mathcal{T}} \int_{\Omega} |\hat{u} - u|^2 dx dt}{\int_{\mathcal{T}} \int_{\Omega} |u|^2 dx dt} \quad \text{and} \quad e_{\Omega}^2(\hat{u}(t), u(t)) = \frac{\int_{\Omega} |\hat{u}(t) - u(t)|^2 dx}{\int_{\Omega} |u(t)|^2 dx}, \quad (10)$$

where the latter local-in-time measure is used to give insight about the error in the spatial domain at a specific time point. We note that if the arguments of the measures are clear from the context we shall simply write  $e_{\Omega \times \mathcal{T}}$  or  $e_{\Omega(t)}$ .

While the two above measures are available in a realistic scenario, we may leverage the fact that the ground truth for our examples is available to define measures on the accuracy of the sub-physics, i.e. the learned missing terms for which no data is assumed. Let  $G(u)$  denote the ground truth term that was used in the neural network's stead when generating the synthetic data. The relative error in sub-physics is then defined as

$$\mathcal{E}^2(u) = \frac{\int_{\mathcal{T}} \int_{\Omega} |\mathcal{N}(u) - G(u)|^2 dx dt}{\int_{\mathcal{T}} \int_{\Omega} |G(u)|^2 dx dt} \quad \text{and} \quad \mathcal{E}^2(u(t)) = \frac{\int_{\Omega} |\mathcal{N}(u(t), t) - G(u(t), t)|^2 dx}{\int_{\Omega} |G(u(t), t)|^2 dx}, \quad (11)$$

where as before the latter term is the relative error at a specific time point  $t$ .

For all examples, we mainly use L-BFGS with line-search for training. This is because our problems have low amounts of data and do not require mini-batching. Additionally, L-BFGS provides superior convergence compared to stochastic gradient descent.

### 3.1. Poisson equation

In this section, we consider the Poisson equation

$$\begin{aligned} \nabla \cdot \kappa \nabla u &= f \quad \text{in } \Omega, \\ u &= g \quad \text{on } \partial\Omega \end{aligned} \quad (12)$$

with  $\Omega = (0, 1)^2$ , source term  $f : \Omega \rightarrow \mathbb{R}$ , solution  $u : \Omega \rightarrow \mathbb{R}$ , and boundary condition  $g : \partial\Omega \rightarrow \mathbb{R}$ . The spatially varying coefficient  $\kappa : \Omega \rightarrow \mathbb{R}$  is assumed unknown.

Using the hybrid FEM-NN approach we shall investigate (i) how the error in the predicted coefficient  $\kappa$  decreases with discretisation error, (ii) sensitivity of the neural network to noise in the observations of  $u$  and (iii) the effect of partial observations of  $u$  on the predictions of the coefficient. In all cases,  $\kappa(x, y)$  was

approximated by a NN  $\mathcal{N}(x, y; W)$  with a single hidden layer consisting of 30 neurons and sigmoid activation functions.

### 3.1.1. Discretisation error

In this case we use a method of manufactured solution, choosing the solution  $u(x, y) = \sin(\pi x) \sin(\pi y)$  as in [9] and diffusion coefficient  $\kappa(x, y) = 2 - x$ . The objective functional is defined as the  $L_2(\Omega)$ -error between the predicted solution of eq. (12) and the true solution on  $\Omega$ .

Using gradually refined meshes  $\Omega_h$  we train five different neural networks  $\mathcal{N}_h \approx \kappa$ . On each mesh the spaces  $U_h = V_h$  are constructed using continuous piecewise-linear ( $P_1$ ) functions<sup>2</sup>. Starting with the same initial weights, all five neural networks are trained for 1 000 iterations of L-BFGS.

The trained neural networks,  $\mathcal{N}_h$ , are then used with a high resolution mesh and piecewise second-order polynomials to produce predicted solutions  $\hat{u}$ . The error in these predicted solutions can be seen in fig. 1 together with the error in the approximated diffusion coefficient. We observe that the error in both the predicted solution and diffusion coefficient decrease quadratically for  $P_1$  elements. The same experiment is repeated using discontinuous  $P_0$  elements, where we observe a close to linear decrease in the error for the predicted diffusion coefficient. These convergence rates are in line with the theoretical rates of convergence for the finite elements used, and suggests that the choice of discretisation is essential for a good NN approximator.

In [11] an upper bound on the approximation error of a NN for a 1-dimensional Poisson problem and  $P_1$  finite elements is derived

$$\|\kappa - \mathcal{N}_h\| \leq C_1 \epsilon + C_2 h^2,$$

where  $\epsilon$  is the optimisation error such that the objective functional is bounded by  $O(\epsilon)$  and  $C_1, C_2$  depend on the data. While the model problem analyzed in [11] is not directly applicable to our problem, the error bound could explain how the error rate of convergence for the diffusion coefficient slows down as  $h$  becomes small for  $P_1$  finite elements. Specifically, it may be that the discretisation error has become so small that the optimisation error  $\epsilon$  is beginning to meaningfully influence the error.

---

<sup>2</sup>We denote by  $P_k$  the space of continuous (Lagrange) finite element functions such that the restriction to (triangular) cell is a polynomial of degree  $k$ .

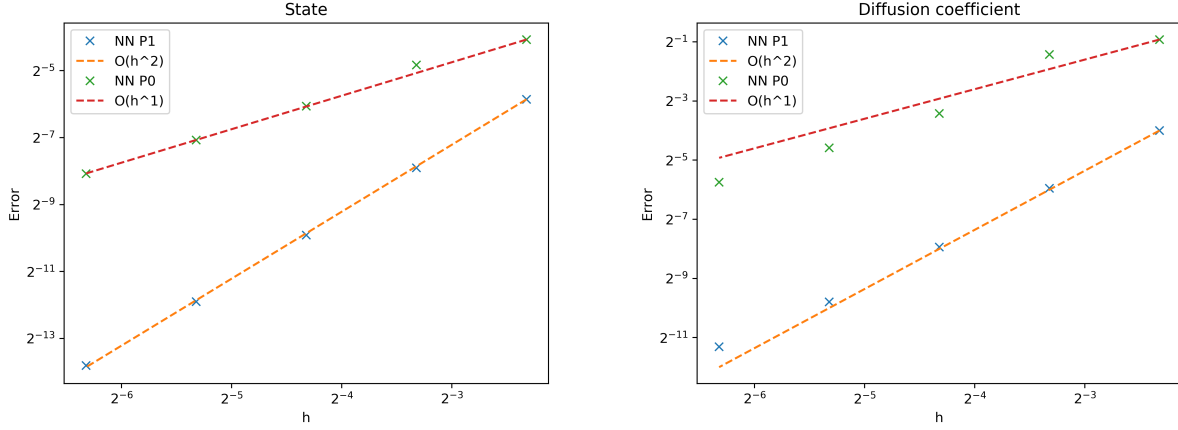


Figure 1: The prediction errors for different mesh resolutions and elements. Left: the  $L_2(\Omega)$ -error in the predicted state when trained on a mesh with distance  $h$  between vertices. The predicted states are produced by using FEM on a high resolution mesh. Right: the  $L_2(\Omega)$ -error in the neural network compared to the true coefficient  $\kappa$ .

### 3.1.2. Noisy observations

We consider the same setup as in the previous example. However, newly additive noise with variance  $\sigma^2$  is applied to the observations such that the signal to loss ratio  $\|u\|/\sigma^2 = 10$  in the  $L_2(\Omega)$  norm. Additionally, we keep the boundary noise-free. Thus, in this instance, our objective functional is defined as

$$L = \|\hat{u} - (u + \epsilon)\|_{L_2(\Omega)}^2,$$

where  $\hat{u}$  is the predicted solution,  $u$  is the observation and  $\epsilon$  is a piecewise linear interpolation of pointwise noise. In particular, at each degree of freedom  $x_i \in \Omega_h$ , we add normally distributed noise  $\epsilon(x_i) \sim \mathcal{N}(0, \sigma^2)$  with variance  $\sigma^2 = \|u\|/10 = 0.025$ . This setup is similar to the one in [9], except with 30 neurons in the hidden layer as opposed to 10. Additionally, we use signal to noise ratio 10 while their example with noisy data has a signal to noise ratio of 100.

Using the same stopping criterion as in [9], that is, the gradient being smaller than  $10^{-6}$ , the L-BFGS algorithm stops at 25 iterations. The resulting trained network can be seen in fig. 2. In this instance, it seems the network makes a fairly good approximation given the amount of noise found in the observations. Although not as accurate as the results in [9], the significantly higher amount of noise is likely the cause. In addition, though the diffusion coefficient  $\kappa(x, y) = 2 - x$  seems simple due to being invariant in  $y$ , this provides an opportunity for the neural network to overfit the noise based on  $y$ .

In [9] it is demonstrated that a neural network provides implicit regularisation, removing the need for  $H^1(\Omega)$  regularisation that is often required for a pointwise estimator. However, the stopping criterion of the gradient norm being smaller than  $10^{-6}$  provides a form of regularisation, as we can see in fig. 2 when training until the norm of the gradient is below  $10^{-7}$ . In particular, neither stopping criterion stops at the

optimal point over the course of training, but the first criterion stops before the network starts overfitting to noise.

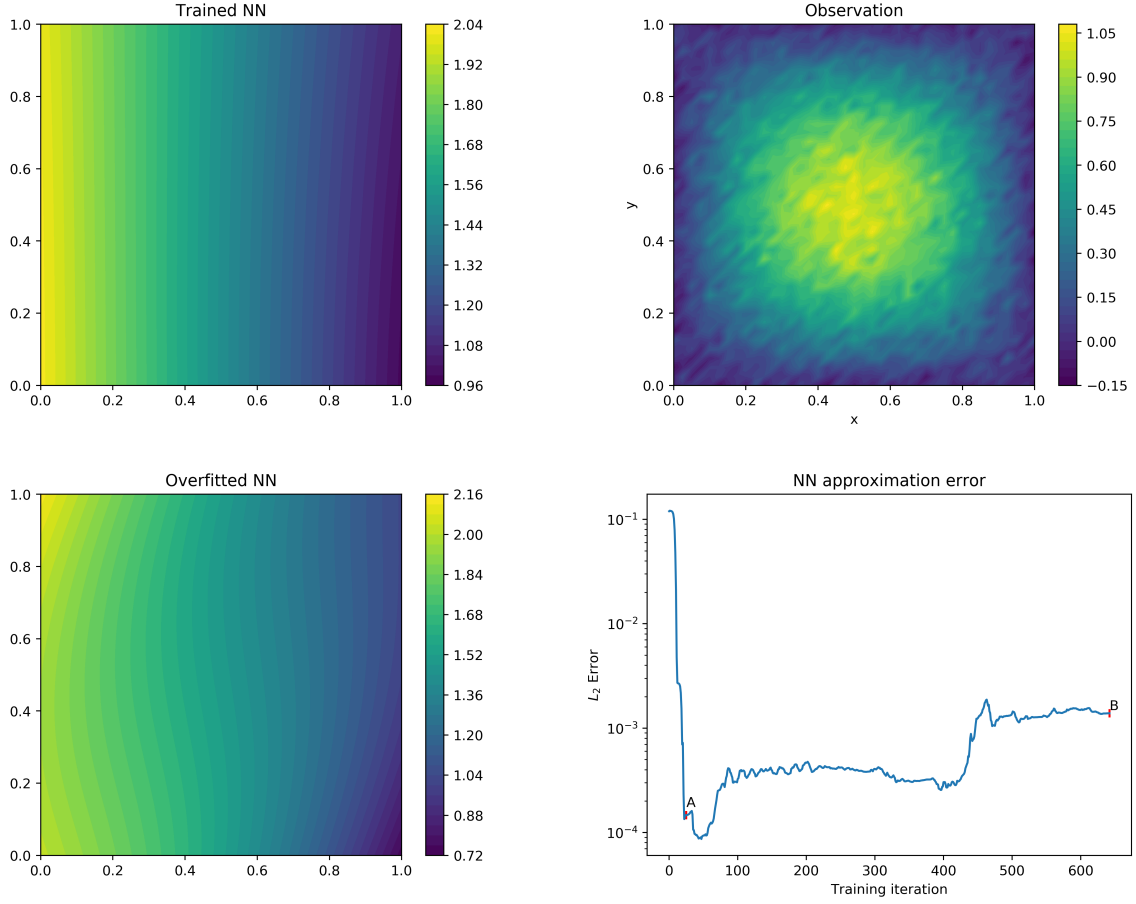


Figure 2: Top left: the trained neural network with stopping criterion at the norm of the gradient below  $10^{-6}$ . Top right: the noisy observation used to train the neural networks. Bottom left: the trained neural network with stopping criterion at the norm of the gradient below  $10^{-7}$ . Bottom right: the  $L_2(\Omega)$  error between the true  $\kappa$  and the intermediate neural network weights during training. The trained neural network stops at point A and the overfitted neural network stops at point B.

### 3.1.3. Partial observations

We consider two problems in which the data are available only in parts of the domain's closure  $\bar{\Omega}$ . First the observations shall be given on a subdomain of  $\Omega$ . In the second example the data is given only on part of the boundary. In both cases  $P_1$  finite element spaces are used.

Consider the subdomain  $D = \{(x, y) \in \Omega : |x - 0.5| \leq 0.25, |y - 0.5| \leq 0.15\}$ , being a rectangle centered at the middle of the unit square with sides of length 0.5 and 0.3. Inside  $D$  we have data on every degree of freedom/vertex of the mesh. We let the solution of eq. (12) be  $u(x, y) = \sin(\pi x) \sin(\pi y)$  and the unknown

diffusion coefficient  $\kappa(x, y) = 1 + \frac{1}{2} \sin(\pi x) \sin(\pi y)$ .

The NN was trained for 10000 iterations of L-BFGS and can be seen in fig. 3. Although the neural network is only provided observations inside the rectangle, it is able to recover an accurate approximation of the true diffusion coefficient  $\kappa$  also outside the box.

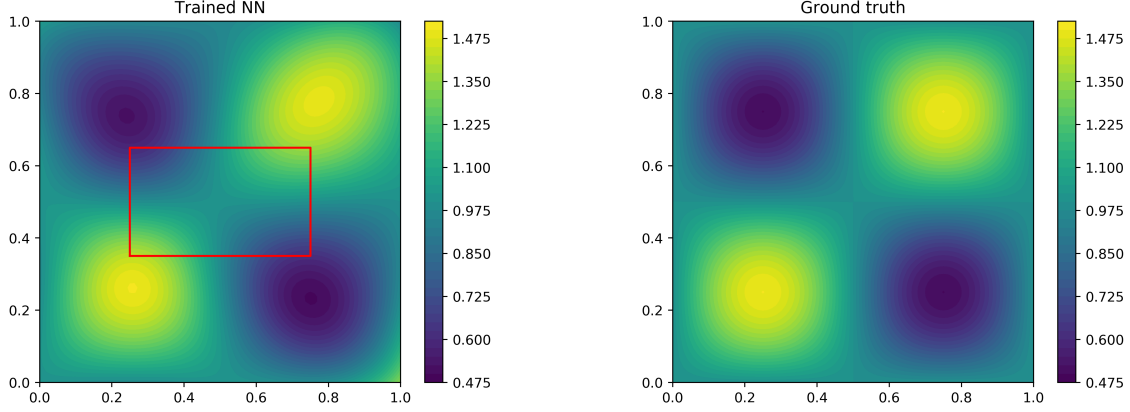


Figure 3: Left: the trained neural network approximating the diffusion coefficient  $\kappa$ . The network was only trained on observations from inside the red box. Right: the true diffusion coefficient  $\kappa$ .

For the second partial observations example we consider the Calderon problem, see [23] and references therein. In this problem, there is no source term,  $f = 0$ , and observations on  $u$ ,  $\kappa \frac{\partial u}{\partial n}$  are given on the boundary  $\partial\Omega$ . Here,  $n$  is the outward directed boundary normal. We remark that that when  $u$  is the voltage potential,  $\kappa \frac{\partial u}{\partial n}$  gives the current flowing through the boundary and the task of recovering  $\kappa$  from the voltage/current measurements is of importance in electrical impedance tomography.

Adopting the example from [23], we define the boundary function as:

$$g(x, y) = e^{-\frac{(x-1)^2 + (y-0.5)^2}{0.5^2}} - e^{-\frac{x^2 + (y-0.5)^2}{0.5^2}} \quad (x, y) \in \partial\Omega,$$

which provides one radial sink term at the middle of the left boundary and a radial source term at the middle of the right boundary. The assumed unknown diffusion coefficient is defined as a radial coefficient

$$\kappa(x, y) = 1 + 4e^{-\frac{(x-0.5)^2 + (y-0.5)^2}{0.2^2}}$$

that attains the value 5 in the center of the unit square and decreases exponentially closer to the boundary. Synthetic data was generated by solving the equation using the FEM with second order polynomials on triangles using the diffusion coefficient  $\kappa$ . The domain was divided into  $2 \times 200^2$  triangles.

In the hybrid FEM-NN approach, the boundary observations on  $u$  are used to enforce the Dirichlet boundary condition in the approximated equation, and the derivative information is used in the loss function

$$L = \|\mathcal{N} \frac{\partial \hat{u}}{\partial n} - \kappa \frac{\partial u}{\partial n}\|_{L_2(\partial\Omega)}.$$

The neural network was first trained for 1 000 iterations of L-BFGS. At this point, due to slow convergence, we switched to the truncated Newton method (TNC) and performed additional 1 000 iterations.

The resulting neural network approximation is shown in fig. 4. Although the neural network is not able to accurately capture the magnitude of the true diffusion coefficient in the center, it is able to capture the radial shape; a significant improvement over the results presented in [23]. Note that the contribution from the second term in  $\kappa$  is on the order of  $10^{-3}$  to  $10^{-5}$  along the boundary.

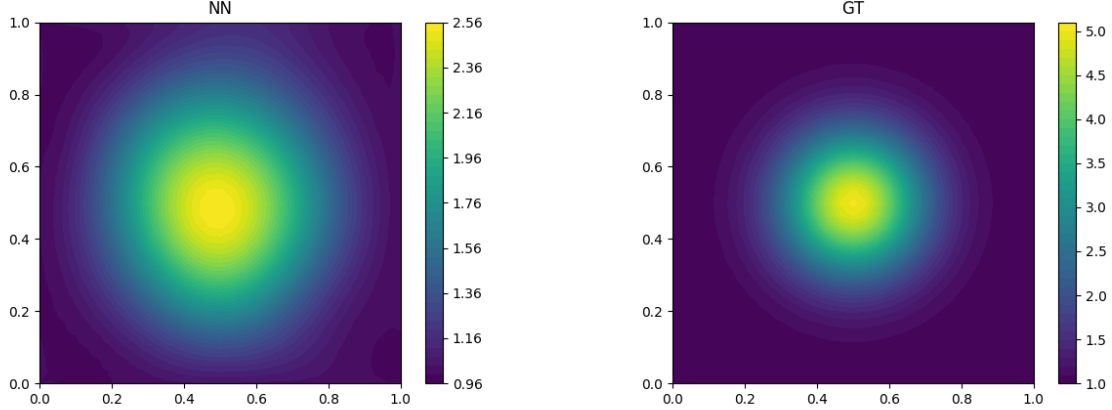


Figure 4: Left: the trained neural network approximation of the diffusion coefficient  $\kappa$ . Right: the true diffusion coefficient  $\kappa$ . The neural network has only been trained on observations on the boundary.

### 3.2. Comparison to other approaches

In this section, we compare the proposed hybrid FEM-NN methodology to physics informed neural networks (PINNs) [5] and pointwise estimation. To this end let us consider an inverse problem for the 1-dimensional heat equation

$$u_t - \nabla \cdot (\kappa \nabla u) = 0 \quad \text{in } \Omega \times (0, T) \quad (13)$$

with  $\Omega = (0, 1)$ ,  $T = 0.1$ . The diffusion coefficient  $\kappa : \Omega \rightarrow \mathbb{R}$  is assumed to be unknown. The problem is closed with an initial condition and homogeneous Dirichlet boundary conditions

$$\begin{aligned} u &= 0 & \text{on } \partial\Omega \times (0, T), \\ u &= u_0 & \text{on } \Omega \times \{0\} \end{aligned}$$

with  $u_0(x) = x(x - 1)$ . Further, we assume  $\kappa > 0$  such that the problem remains well-posed.

We apply PINNs and FEM-NN to reconstruct two different choices for the diffusion coefficient  $\kappa$ : a linear case and a discontinuous piecewise constant case. Here, the linear case admits a smooth solution  $u$  and functions as a basic benchmark for our comparison. The discontinuous diffusion coefficient results in a more

challenging problem, which, however is highly relevant e.g. in biomechanics [24]. More precisely, the solution is not smooth, with jumps in the gradients at the points of the (coefficient) discontinuity.

For each case, synthetic data is generated by solving the equation using a high resolution FEM discretisation in space and explicit first stage implicit 4th order Runge Kutta (ESDIRK43a) as described in [25]. We employed the ESDIRK43a implementation provided in the gryphon-project [26]. The spatial interval is divided into  $N_x = 4096$  sub-intervals and the time step was kept fixed at  $\Delta t = 10^{-4}$ . Finally, the set of training observation times is  $\mathcal{T} = \{i\tau\}_{i=1}^5$  where  $\tau = 0.02$  is the temporal spacing between (equispaced) observation snapshots.

In the hybrid FEM-NN approach, we replace the unknown term  $\kappa$  by a neural network  $\mathcal{N}(\cdot; W) : \Omega \rightarrow \mathbb{R}$  with a single hidden layer, hyperbolic tangent activation functions, and weights  $W$ . The hidden layer has 30 neurons. The problem equation then reads

$$\begin{aligned} \hat{u}_t - \nabla \cdot (\mathcal{N}(\cdot; W) \nabla \hat{u}) &= 0 \quad \text{in } \Omega \times (0, T), \\ \hat{u} &= 0 \quad \text{on } \partial\Omega \times (0, T), \\ \hat{u} &= u_0 \quad \text{on } \Omega \times 0. \end{aligned} \tag{14}$$

Problem eq. (14) is solved using FEM in space and Crank-Nicolson in time. The domain  $\Omega$  is discretised into 240 sub-intervals and the  $P_1$  finite elements are used. We remark that the test functions in  $V$  satisfy the (homogeneous) Dirichlet boundary conditions by construction. Further, we use  $\Delta t = 2.5 \times 10^{-3}$  that coincides with the observation time points. The variational problem formulation with function space  $V$  reads: Given  $\hat{u}^0 = u_0$  for  $n = 1, 2, \dots$  find  $u^n \in V$  such that

$$\int_{\Omega} \frac{\hat{u}^{n+1} - \hat{u}^n}{\Delta t} \cdot v + \frac{\mathcal{N}(\cdot; W)}{2} (\nabla \hat{u}^{n+1} + \nabla \hat{u}^n) \cdot \nabla v \, dx = 0 \quad \forall v \in V \tag{15}$$

with  $\hat{u}^n = \hat{u}(x, n\Delta t)$ . Hence, the inverse problem formulation in the hybrid FEM-NN model becomes

$$\min_{W, \hat{u}} \sum_{t_i \in \mathcal{T}} \int_{\Omega} (\hat{u}(x, t_i) - u(x, t_i))^2 \, dx + \alpha \int_{\Omega} (\mathcal{N}(x; W))^2 \, dx \text{ subject to eq. (15)}. \tag{16}$$

Here  $\alpha > 0$  is an  $L^2(\Omega)$  regularisation parameter for the neural network. This regularisation is added due to the inverse problem being ill-posed, see [27]. For our problems we choose a regularisation parameter  $\alpha = 10^{-6}$ .

We remark that the positivity constraint  $\kappa \approx \mathcal{N} > 0$  is only ensured during initialization of the weights  $W$  before training. Although  $\mathcal{N}$  could violate the positivity constraint during training, we did not encounter this problem for the results presented below. In those cases, one could consider using ReLU or a smooth approximation to ReLU on the output to enforce the constraint by construction.

The pointwise estimator approach uses the same formulation of the inverse problem as eq. (16), except that the neural network  $\mathcal{N}$  is replaced by an unknown  $P_1$  function over the (same) mesh of  $\Omega$ .

The PINN approach does not use a variational formulation of the problem, and instead incorporates eq. (14) as penalty to the minimisation problem. The solution of eq. (14) is approximated using a neural network  $\hat{u}(x, t) = \mathcal{N}_2(x, t; W_u)$  parameterized by  $W_u$ . This network consists of 3 hidden layers with 16 neurons each and hyperbolic tangent activation functions. The inverse problem in the PINN case reads

$$\min_{W, W_u} \sum_{t_i \in \mathcal{T}} (\hat{u}(x, t_i; W_u) - u(x, t_i))^2 + \alpha(\mathcal{N}(x; W))^2 + L_{\text{pde}}(\hat{u}(\cdot, \cdot; W_u)). \quad (17)$$

Here  $L_{\text{pde}}$  measures the residual of eq. (14) point-wise at collocation points

$$L_{\text{pde}}(\hat{u}) = w_{\text{int}} F(\hat{u}) + w_{\text{bc}} L_{\text{BC}}(\hat{u}) + w_{\text{ic}} L_{\text{IC}}(\hat{u}),$$

where  $F$  is the  $l^2$  residual of the PDE in the interior

$$F(\hat{u}) = \sum_{(x, t) \in \mathcal{X}_{\text{int}}} (\hat{u}_t(x, t) - \nabla \cdot \mathcal{N}(x; W) \nabla \hat{u}(x, t))^2$$

and

$$L_{\text{BC}}(\hat{u}) = \sum_{(x, t) \in \mathcal{X}_{\text{bc}}} (\hat{u}_t(x, t))^2, \quad L_{\text{IC}}(\hat{u}) = \sum_{x \in \mathcal{X}_{\text{ic}}} (\hat{u}_t(x, 0) - u_0(x))^2$$

enforce the boundary and initial conditions. Sets  $\mathcal{X}_{\text{int}}, \mathcal{X}_{\text{bc}}, \mathcal{X}_{\text{ic}}$  are the sets of collocation points in the interior, boundary and for the initial condition respectively. Further,  $w_i, i = \{\text{int}, \text{bc}, \text{ic}\}$  are weights balancing the different terms in the loss function and we set  $w_i = 1/|\mathcal{X}_i|$ . Finally, we sample the collocation points in a regular grid with 241 points in  $\Omega$ , i.e. the vertices of the finite element mesh, and 40 points in  $[0, T]$ .

We note that the form of PINNs considered further is that from the original paper [5]. However, the method has seen a rapid development with a number of PINN variants (e.g. [28, 29]), training methods [30] or architectures [31] proposed, which would likely improve its performance on our benchmark problems. We chose the original implementation simply as a point of reference.

### 3.2.1. Linear diffusion coefficient

Let the diffusion coefficient be defined as

$$\kappa(x) = 2x + 1.$$

In the hybrid approach, eq. (16) is optimised using SciPy L-BFGS-B [32, 33] for 100 iterations. The point-wise estimator is trained for 1 000 iterations of L-BFGS-B. For the PINN approach, eq. (17) is optimised using 100 000 and 1 000 000 iterations of L-BFGS-B. The PINN optimisation approach requires significantly more training iterations, which is not surprising because there are two neural networks being trained simultaneously: the unknown diffusion coefficient for the inverse problem and the solution of the PDE given the current estimate of the diffusion coefficient. However, note that the forward and backpropagation of the PINN model is faster than for the hybrid model.

The trained networks are plotted in fig. 5. We observe that both the hybrid and PINN method are able to recover an accurate approximation of the unknown diffusion coefficient  $\kappa$ . However, even after 100 000 iterations, the PINN trained network has quite a significant error compared to the true  $\kappa$ , whereas this error is significantly reduced if the networks are trained for ten times longer.

The wall clock run times for the training were roughly 1 minute for the hybrid model, a bit under 2 hours for 100 000 iterations and roughly 18 hours for 1 000 000 iterations of training the PINNs. All training is performed on a CPU, but we would not expect much better performance on a GPU due to the NNs being small. Thus, the hybrid approach clearly outperforms the PINN method in this simple test problem, both in terms of training time and in accuracy of the solution. This advantage comes mainly from the PINN approach involving two neural networks that balance each other during training. In other words, the data terms and PDE term in eq. (17) can only decrease with small decrements because a decrease in one term will likely cause an increase in the other term. We remark that the use of adaptive activation functions [31] or adaptive learning rates [30] in PINNs would likely speed up convergence.

Further, observe that in fig. 5 the pointwise estimator is not able to accurately recover the diffusion coefficient. Although the error in the solution  $u$  is actually lower than for the hybrid method, the pointwise estimator produces a non-smooth solution to the inverse problem. This is in line with previous results in [9, 12], where it is shown that the neural network can act as regularisation and produces smooth approximations. It should be noted that the number of degrees of freedom used for the pointwise estimator is significantly greater than the number of weights in the neural network. Specifically, the pointwise estimator has 241 degrees of freedom while the neural network has 91.

Since  $L^2$ -regularisation results in an oscillating pointwise estimator, we attempt to impose higher regularity on the estimated solution by replacing the  $L^2$ -regularisation with  $H_0^1$ -regularisation:

$$\alpha \int_{\Omega} |\nabla \mathcal{N}(x)|^2 \, dx,$$

where  $\mathcal{N}$  is the pointwise estimator and  $\alpha$  remains the same at  $\alpha = 10^{-6}$ . The resulting estimator can be seen in fig. 5. It accurately reconstructs the linear diffusion coefficient, and is comparable to the hybrid and PINN method. Furthermore, the pointwise estimator converges in less than 100 iterations of L-BFGS-B, outperforming both PINN and the hybrid method in terms of time spent training. However, it still has slightly higher error than the PINN trained for 1 000 000 iterations. This error could likely be further reduced by tuning the regularisation parameter  $\alpha$ .

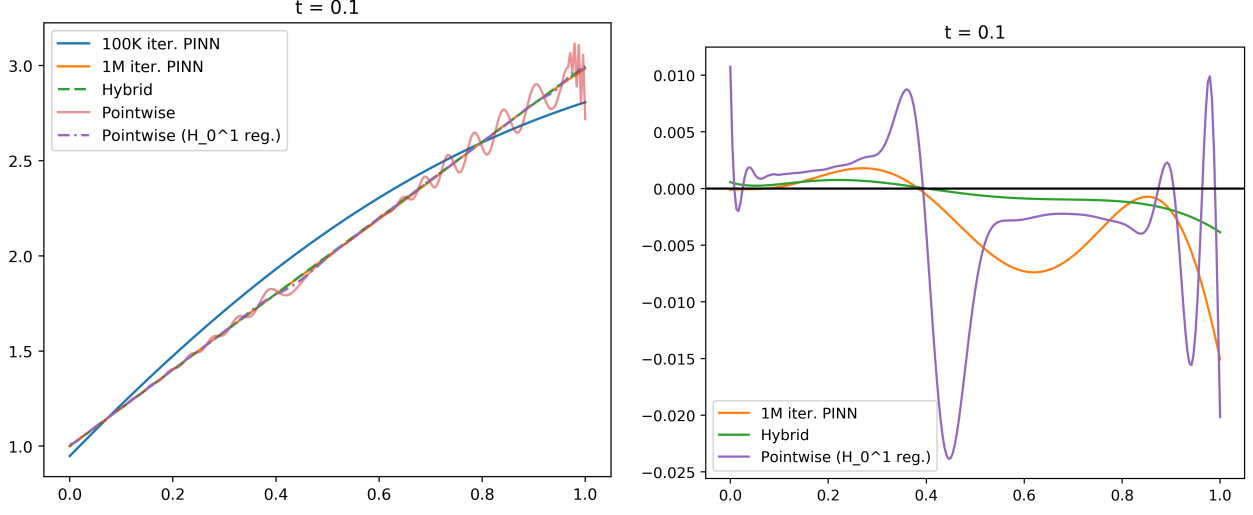


Figure 5: Left: the trained neural networks as well as the pointwise estimators of the linear diffusion coefficient  $\kappa$ . The hybrid method, PINNs after 1 million iterations, and the pointwise estimator with  $H_0^1$  regularisation are able to accurately approximate  $\kappa$ . Right: the error  $\mathcal{N} - \kappa$  for the trained neural networks from the hybrid method and the PINN method after 1 million iterations, in addition to the pointwise estimator with  $H_0^1$  regularisation.

### 3.2.2. Discontinuous diffusion coefficient

Let the diffusion coefficient be piecewise constant

$$\kappa(x) = \begin{cases} 2 & |x - 0.5| \leq 0.25 \\ 1 & \text{otherwise} \end{cases}.$$

For this case the discontinuity cannot be captured by the point-wise approach used in PINNs, and using our previous residual formulation would result in the equation  $\hat{u}_t/\kappa - \nabla \cdot \nabla \hat{u} = 0$ . To mitigate this, we use the following mixed problem formulation for our PINN approach

$$\begin{aligned} \hat{u}_t - \nabla \cdot \phi &= 0 && \text{in } \Omega, \\ \phi - \kappa \nabla \hat{u} &= 0 && \text{in } \Omega, \end{aligned}$$

where the new variable, flux  $\phi$ , is approximated by a third neural network  $\mathcal{N}_3(x, t; W_\phi)$ . This neural network has the same structure as the PDE solution network  $\mathcal{N}_2$ . This formulation results in the following PINN PDE residual

$$F(\hat{u}) = \sum_{(x,t) \in \mathcal{X}_{\text{int}}} \left[ (\hat{u}_t(x, t) - \nabla \cdot \mathcal{N}_3(x, t; W_\phi))^2 + (\mathcal{N}_3(x, t; W_\phi) - \mathcal{N}(x; W) \nabla \hat{u})^2 \right].$$

This time around, the hybrid model does not converge as fast, and we train for 1 000 iterations of L-BFGS-B followed by 1 000 iterations of TNC. The pointwise estimator is trained for 1 000 iterations of L-BFGS-B.

Finally, the PINN is trained for 1 000 000 iterations of L-BFGS-B. The solution, at  $t = 0.1$ , of eq. (14) with the trained neural networks, using the same discretisation scheme as was used to generate the synthetic data, can be seen in fig. 6. The solution plot is only over the interval  $[0.2, 0.8]$  to highlight the differences between the predicted solutions, since the solutions match the reference solution well outside of this interval.

In this case, we observe that the hybrid model is able to capture the discontinuities in  $\kappa$  that cause a kink in the state. Meanwhile, the PINN method seems to instead only provide a smooth approximation to the discontinuous  $\kappa$ , resulting in a state that also is smooth. It is worth mentioning that the hybrid model produces similar results as PINN in the early phases of training, indicating that PINNs could attain similar results. That said, we see only slight improvement by increasing the number of training iterations from 100 000 to 1 000 000. However, given the discontinuity a variant of PINN which is better suited for the problem is the extended PINN [29]. Here,  $u$  and  $\kappa$  would be represented by several “subdomain” networks coupled accross the interfaces, some of which could be the points of discontinuity, thus making it possible to capture the non-smooth coefficient. At the same time, of the discontinuity might not be known a priori.

In fig. 7 the hybrid and PINN loss functions are plotted along log scaled axes. While the PINN data loss, which includes regularisation, attempts to measure the same misfit as the hybrid loss, the two quantities are not directly comparable as one is an integral and the other is the mean over the collocation points. Additionally, the reported loss for the PINN is based on the neural network approximation of the state, which might not reflect the actual solution with the current estimate for the diffusion coefficient  $\kappa$ . Nevertheless, we can see that the PINN loss steadily decreases, but that it will likely take over 10 million iterations to reduce the loss below  $10^{-4}$ .

We remark that the neural network used to approximate  $\kappa$  is capable of approximating the discontinuous function more accurately than what is found by the hybrid method. Thus, it is reasonable to assume that the hybrid model could be trained further to improve the approximation of  $\kappa$ .

On the other hand, the pointwise estimator predicts a very irregular estimate of  $\kappa$  when using  $L^2$ -regularisation. Thus, as before, we train the pointwise estimator using  $H_0^1$ -regularisation. The resulting estimate of the discontinuous coefficient  $\kappa$  can be seen to the right in fig. 6. Again the pointwise estimator with  $H_0^1(\Omega)$ -regularisation produces a fairly good estimate of the unknown diffusion coefficient  $\kappa$ . While the error is still slightly higher than the hybrid method, the pointwise method converges much faster: at around 2 minutes versus 2 hours for the hybrid method.

Although pointwise estimators might be a viable or even better alternative to the hybrid method with an unknown spatially varying coefficient like in eq. (16), pointwise estimation is not suited for inverse problems where the unknown term is a differential operator or depends on the state in a nonlinear way. We shall next address this type of learning with a hybrid approach.

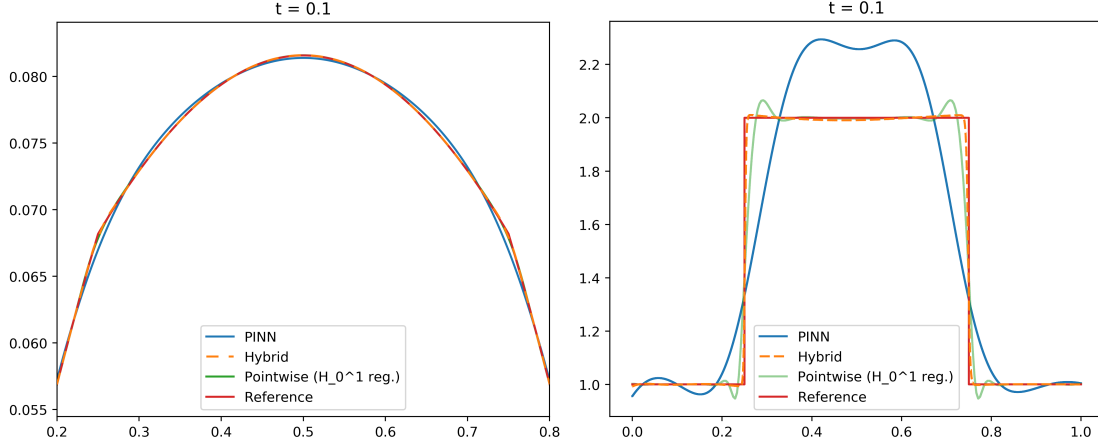


Figure 6: Left: the approximated solution at  $t = 0.1$  of eq. (14) with the trained neural networks as well as the pointwise estimator. The plot is limited to the interval  $[0.2, 0.8]$  to highlight the differences in the solutions. Right: the approximations of  $\kappa$  by the trained neural networks and the pointwise estimator.

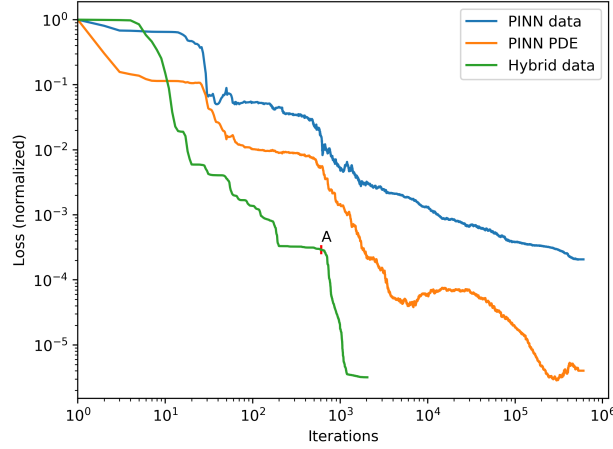


Figure 7: The normalized loss functions over number of training iterations in a log-log plot. The losses are normalized such that the first iteration is 1. Beyond point A we switch the training of the hybrid method from L-BFGS-B to the truncated Newton method. It is important to note that few iterations of truncated Newton involve many function evaluations due to inner conjugate gradient iterations.

### 3.3. Advection-diffusion equation

For this example, we consider the advection-diffusion equation given by

$$u_t - D\Delta u + \nabla \cdot (\omega u) = 0 \quad \text{in } \Omega \times (0, T), \quad (18)$$

where  $\Omega \subset \mathbb{R}^d$ ,  $D$  is a diffusion constant and  $\omega : \Omega \rightarrow \mathbb{R}^d$  is the advection velocity. Boundary and initial conditions completing eq. (18) shall be specified later.

Treating the advection term as unknown, the learning problem solves the following equation

$$\hat{u}_t - D\Delta\hat{u} + \mathcal{N}(\hat{u}, \nabla\hat{u}; W) = 0 \quad \text{in } \Omega \times (0, T) \quad (19)$$

with  $\mathcal{N}(\cdot; W) : \mathbb{R} \times \mathbb{R}^2 \times \Omega \rightarrow \mathbb{R}$  a neural network parameterized by the weights  $W$ . That is, we supply the neural network with the approximated state  $\hat{u}(x, t)$ , first order spatial derivative information  $\nabla\hat{u}(x, t)$ , and the spatial coordinates  $x$ . No information about the advection velocity is available a priori.

Letting  $\Omega = (0, 1)^2$ , synthetic data was obtained by solving eq. (18) with  $D = 0.1$ ,  $\omega(x, y) = [\cos(5(y - 0.5)^2), 0]$ , and  $T = 5.0$  with initial condition  $u(\cdot, 0) \equiv 0$  using  $tP_1$  elements on a grid with  $2 \times 100 \times 100$  elements. On the inlet boundary  $x = 0$  we prescribed Dirichlet boundary conditions  $u = \sin^2(t)$  while on the remaining boundaries Neumann boundary conditions  $\nabla u \cdot n = 0$  were imposed. For the temporal discretisation we use the 4th order implicit Runge Kutta with an explicit first stage [25], as implemented in the gryphon-project [26], with time step  $\Delta t = 0.001$ .

For training, the generated synthetic data was sub-sampled in time with a uniform time-step of 0.2, resulting in 26 observations including the initial condition. The set of time points for these training samples is denoted by  $\mathcal{T}$ . Equation (19) was solved using  $P_1$  elements on a mesh with  $2 \times 30 \times 30$  triangular elements and the Crank-Nicolson scheme with time-step  $\Delta t = 0.1$ . As the initial and boundary conditions, and diffusion coefficient  $D$  are assumed known the learning problem becomes

$$\min_{W, \hat{u}} \sum_{t_i \in \mathcal{T}} \|\hat{u}(\cdot, t_i) - u(\cdot, t_i)\|_{L^2(\Omega)}^2 \quad \text{subject to eq. (19).} \quad (20)$$

For this example, we let  $\mathcal{N}$  be a neural network with one hidden layer, consisting of 30 neurons, with tanh activation functions. The network is trained using scipy L-BFGS-B and TNC. The trained neural network is then used to solve eq. (19) using the same discretisation scheme as was used to generate the synthetic data. Figure 8 shows the resulting predicted solution at  $t = 0.3$  and  $t = 3.5$ . When evaluating the trained neural network with the ground truth discretisation scheme, the computed errors are  $e_{\Omega \times \mathcal{T}}(\hat{u}) = 0.01\%$  in the predicted state and  $\mathcal{E}_{\Omega \times \mathcal{T}}(\mathcal{N}) = 1.0\%$  in the predicted advection term.

To evaluate the temporal extrapolation abilities of the model we compute the state error  $e_{\Omega}(t)$  beyond the training interval  $(0, T)$  with the results shown in fig. 9. We note that the relative error is largest close to 0 as the state is zero here. Beyond the training interval, for  $t > T$  we observe that the error stays below 0.06% and oscillates with the same period as the inlet  $\sin^2(t)$ . Note that even though we only plot to  $t = 50$ , we observe no significant deviations from this pattern even at  $t = 1000$ . This result is not very surprising, because after  $t = 5$  the state  $u(x, t)$  at each point  $x \in \Omega$  will be in the same range as  $u(x, t)$  for  $t < 5$ .

We can get a picture of how well the neural network approximates the velocity  $\omega$  in the advection term  $\nabla \cdot (\omega u)$  by supplying specific state gradients  $\nabla u$ . Since the true velocity only has an  $x$ -component, we plot  $\mathcal{N}(u, \nabla u, x)$  over the spatial coordinates  $x \in \Omega$  with  $u = 0$  and  $\nabla u = (1, 0)$ . The plot together with the true velocity can be seen in fig. 10. The trained neural network seems to reproduce the true velocity field quite

well, however, the neural network is not independent of  $u$  nor the  $y$ -component of  $\nabla u$ , even though this is the case for the true advection operator. Thus, we would get a poor approximation of the velocity field when choosing  $u = 10$  for example, as this is far outside of the range of values in the training data.

To further investigate the accuracy of the trained network, we consider the same equation with a new Dirichlet boundary condition on the inlet boundary. The amplitude is increased from 1 to 4 and the frequency reduced to arrive at  $4\sin^2(0.5t)$ . While the reduced frequency reduces the absolute value of the gradient, it increases the total quantity of substance coming through the inlet over the time interval  $(0, T)$ . Using the neural network that was trained on the old Dirichlet boundary condition, we solve eq. (19) and measure the error against the ground truth. In fig. 11 the predicted solutions at  $t = 0.3, 3.5$  are illustrated. The relative error on the test set is  $e_{\Omega \times \mathcal{T}} = 0.2\%$  for the full model, and  $\mathcal{E}_{\Omega \times \mathcal{T}} = 3.9\%$  for the sub-physics.

The same setup is repeated for an even bigger inlet amplitude at  $16\sin^2(0.5t)$ . Then the relative error is  $e_{\Omega \times \mathcal{T}} = 0.50\%$  for the full model, and  $\mathcal{E}_{\Omega \times \mathcal{T}} = 23\%$  for the sub-physics. A plot for the states at  $t = 0.3, 3.5$  when using this inlet can be seen in fig. 12.

To uncover the reason for this high error in the sub-physics, we leverage the fact that the ground truth term  $\nabla \cdot (\omega u)$  should be linear in  $\partial u / \partial x_1$ . Using the true solution  $u$  of eq. (18) with the new Dirichlet boundary condition, we plot the value of the true advection term together with the predicted advection term from the neural network at a single point  $x$ . As seen in fig. 13, the neural network performs well when  $\partial u / \partial x_1$  has the same magnitude as the training set. Due to the much higher values introduced with the increased amplitude at the inlet boundary, the neural network starts performing poorly, yielding high error.

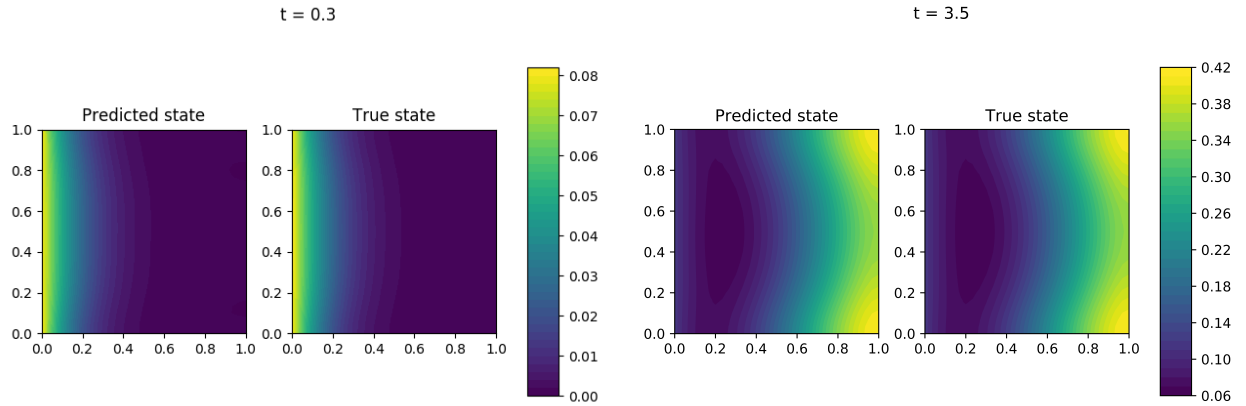


Figure 8: Left: the predicted solution of eq. (19) at  $t = 0.3$  with the fully trained NN, and the true solution at  $t = 0.3$  based on eq. (18). The relative error,  $e_{\Omega}(0.3)$ , is 0.071%. Right: the predicted solution of eq. (19) at  $t = 3.5$  with the fully trained NN, and the true solution at  $t = 3.5$  based on eq. (18). The relative error,  $e_{\Omega}(3.5)$ , is 0.054%

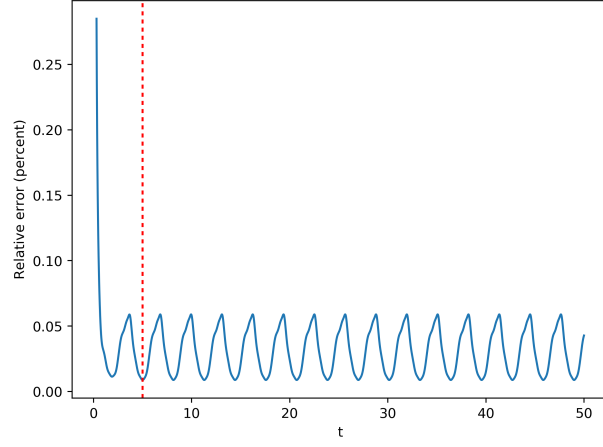


Figure 9: The state error  $e_{\Omega}(t)$  over time. The red line indicates the end of the training interval  $(0, T)$ .

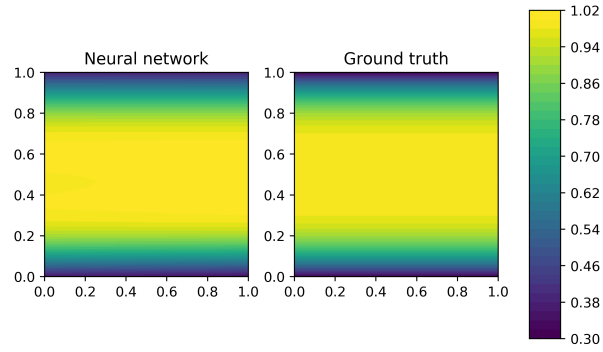


Figure 10: Left: the neural network solution over the spatial domain  $\Omega$  with constant  $u = 0$  and  $\nabla u = (1, 0)^T$  to extract the predicted velocity field. Right: ground truth velocity field over the spatial domain  $\Omega$ .

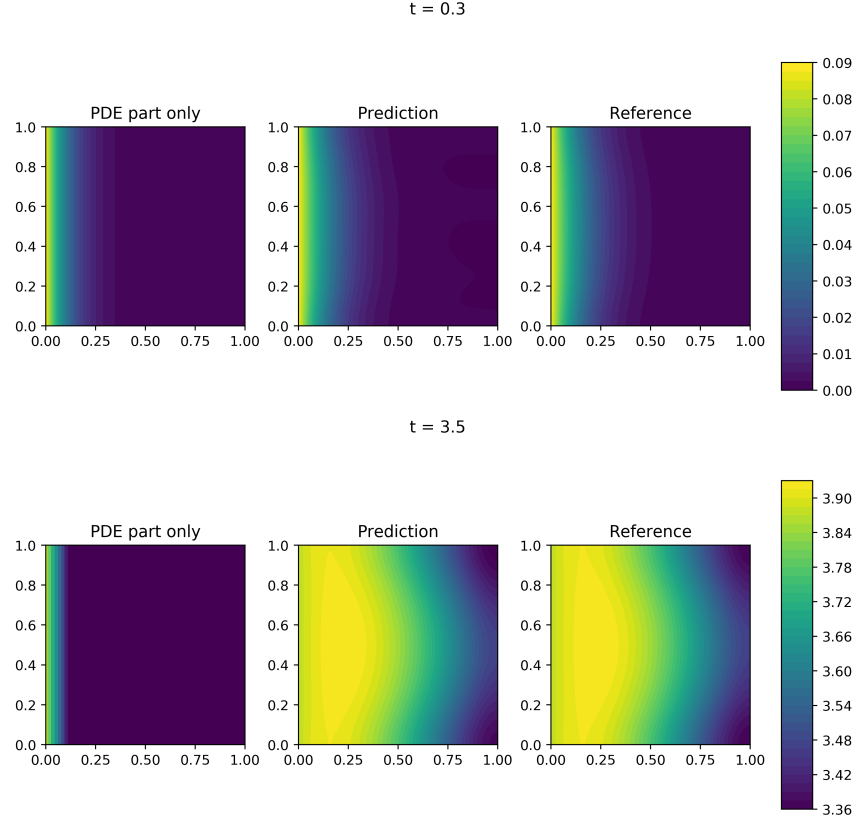


Figure 11: The predicted and true solution of eq. (19) with a new (unseen) Dirichlet boundary condition with amplitude 4. On the left the solution using only the PDE part is included ( $\mathcal{N} \equiv 0$ ). Top: the predicted and true states at  $t = 0.3$ . The relative error,  $e_{\Omega}(0.3)$ , is 0.2%. Bottom: the predicted and true states at  $t = 3.5$ . The relative error,  $e_{\Omega}(0.3)$ , is 0.08%.

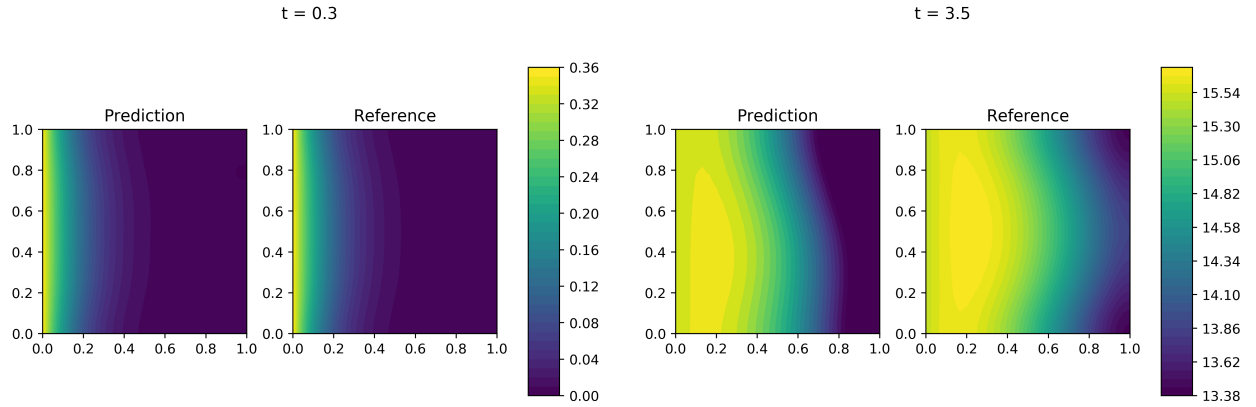


Figure 12: The predicted and true solution of eq. (19) with a new (unseen) Dirichlet boundary condition. Left: the predicted and true states at  $t = 0.3$ . The relative error,  $e_{\Omega}(0.3)$ , is 0.1%. Right: the predicted and true states at  $t = 3.5$ . The relative error,  $e_{\Omega}(0.3)$ , is 3.8%.

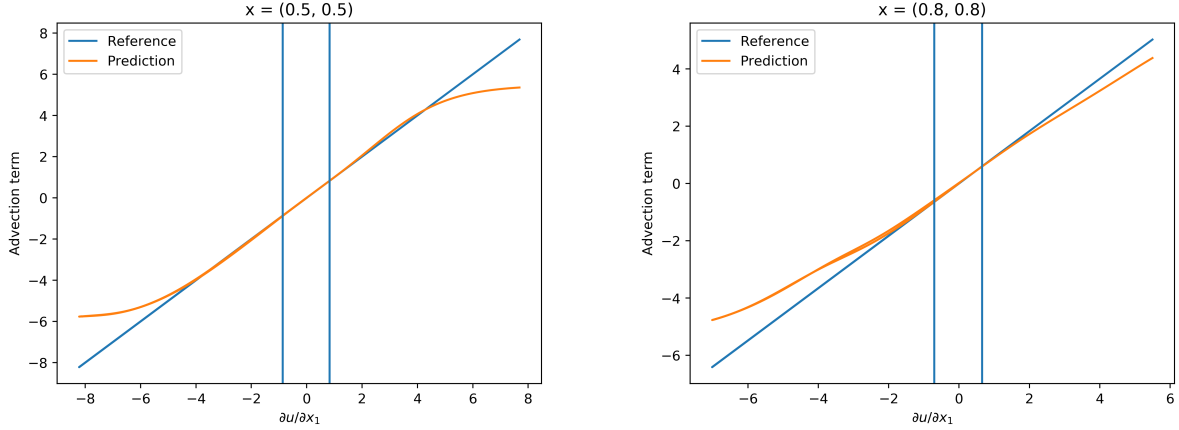


Figure 13: The true and predicted advection term over the range of  $u(x, t)$  for a specific  $x$ . The range within the two vertical lines is the span of the training set. Left: the advection term in the middle of the domain at  $x = (0.5, 0.5)$ . Right: the advection term at  $x = (0.8, 0.8)$ .

### 3.4. Cardiac electrophysiology

Following [34, Ch 2.2] we consider a mathematical model of excitable cardiac tissue describing evolution of the transmembrane potential  $v$  by the coupled PDE-ODE system

$$v_t - \nabla \cdot (M \nabla v) = I_s - I_{\text{ion}}(v, s) \quad \text{in } \Omega \times (0, T), \quad (21a)$$

$$s_t = F(v, s) \quad \text{in } \Omega \times (0, T). \quad (21b)$$

Here  $M$  is the conductivity tensor of the monodomain equation eq. (21a) and  $I_s$  is a given stimulus current. The term  $I_{\text{ion}}$  is the ionic current describing a response of the cardiac cell with the (internal) state  $s(x, t)$  which evolves according to eq. (21b).

The functions  $I_{\text{ion}}$  and  $F$  are specific to a given cell model [35] as they describe the cell's dynamics. However, which properties of the cell are relevant for its electrical behavior and how those properties interact, is a difficult problem and there exists a plethora of cardiac models, see eg. [34, Ch 2.4]. It is thus reasonable to consider a setting where  $F$  and  $I_{\text{ion}}$  would be learnt from data of a specific patient. Therefore, in the following  $F$  and  $I_{\text{ion}}$  are assumed unknown. However, we shall maintain the coupling between the terms as in eq. (21). That is,  $F$  and  $I_{\text{ion}}$  interact via state vector  $s$  and are tied to the monodomain equation by the transmembrane potential.

For our experiments, the model parameters, observations and ground truth are determined by using the Beeler-Reuter model [36]. The decoupled problem is considered, in which the PDE and ODEs are solved separately through a Marchuk-Yanenko splitting scheme. Specifically, in order to advance from  $t_n$  to  $t_{n+1}$

with the timestep  $\Delta t = t_{n+1} - t_n$ , the PDE

$$\frac{v^{n+1} - v^n}{\Delta t} - \nabla \cdot (M \nabla v^{n+1}) = I_s - I_{\text{ion}}(v^n, s^n) \quad \text{in } \Omega,$$

where  $v^n = v(\cdot, t_n)$  and  $s^n = s(\cdot, t_n)$ , is first solved using finite elements. Then, the system of ODEs is solved using an explicit Euler scheme

$$s^{n+1} = s^n + \Delta t F_i(v^{n+1}, s^n).$$

Synthetic data was generated using this scheme on finite elements and a uniform timestep of  $\Delta t = 10^{-3}$ .

The goal of this example, is to approximate both  $I_{\text{ion}}$  and  $F$  using NNs, trained on observations of only  $\{v(x, \tau_i)\}_i$  for a given initial potential  $v(x, 0)$ . We construct the hybrid model such that it has the same number of cell states as in the Beeler-Reuter model. Both NNs take in only  $v$  and  $s$  evaluated at a point  $(x, t) \in \Omega \times (0, T)$ , and are not provided any spatial or temporal coordinates, nor any derivative information. The same scheme as was used to generate synthetic data was used for training the hybrid model. However, the time step in training was larger at  $\Delta t = 0.01$ . Furthermore, both neural networks are implemented in PyTorch and interpolated at the finite element mesh vertices.

Although estimation of  $s(x, 0)$  from observations of  $v$  might be possible using a NN as suggested in [37], the hybrid model assumes that  $s(x, 0)$  is zero for simplicity. Thus, one cannot expect a reconstruction of any meaningful cell states.

The forcing term is approximated by a feedforward NN with 3 hidden layers that have 64, 128, and 64 neurons. The ionic current term is approximated by a feedforward NN with 6 hidden layers utilizing skip connections between the 3rd and 5th layer, 2nd and 6th layer, and 1st and 7th layer. The hidden layers have 64, 128, 256, 512, 256, 128, 64 neurons. Hyperbolic tangent activation functions were used in both NNs.

The predicted state after training the NNs can be seen in fig. 14 together with the predicted ionic current term  $-I_{\text{ion}}$ . We observe that the transmembrane potential  $v$  is accurately recovered even when we use a smaller timestep than under training  $\Delta t = 10^{-3}$ . However, looking at the ionic current term the network seems to have difficulties reproducing the spike, instead producing an average over that timespan. This inaccuracy does not seem to cause any issues in the predicted state.

While the model was trained with no external stimulus  $I_s = 0$ , we test the trained NN when an exponentially decreasing stimulus is introduced after 10 time units,

$$I_s(x, t) = \begin{cases} 0 & t < 10 \\ 50e^{9-t} & t \geq 10 \end{cases}.$$

The prediction with this external stimulus can be seen in fig. 15. While the NNs are able to capture the true  $v$  for a small window after the stimulus is applied, it overshoots as the transmembrane potential starts decreasing. Note that the curve at the end of the interval resembles the one the networks are trained on.

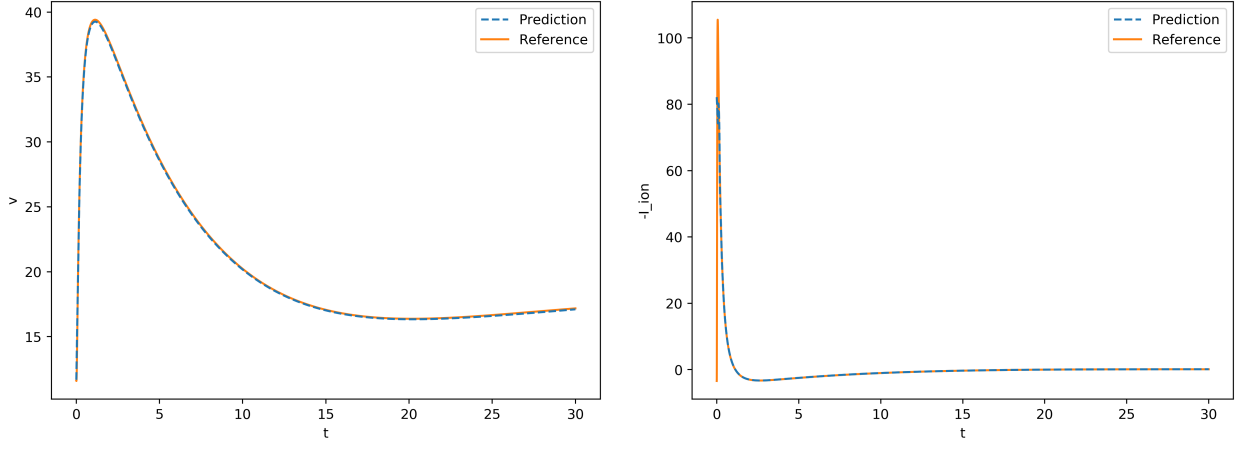


Figure 14: Left: the predicted and true state  $v$  at  $x = (0.5, 0.5)$  over time. Right: the predicted and true  $-I_{\text{ion}}$  term at  $x = (0.5, 0.5)$  over time.

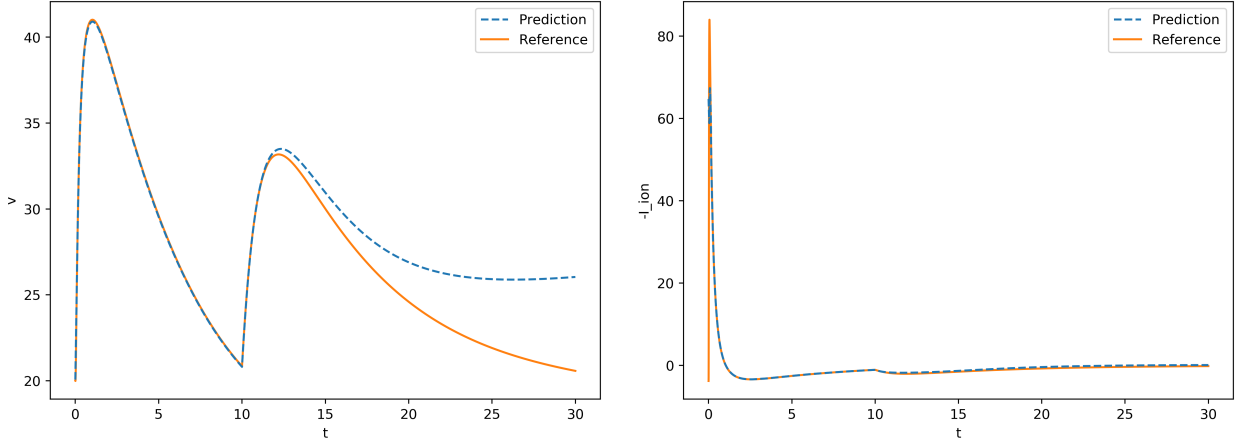


Figure 15: The trained hybrid FEM-NN model with non-zero  $I_s$  after 10 time units. Left: the predicted and true state  $v$  at  $x = (0.5, 0.5)$  over time. Right: the predicted and true  $-I_{\text{ion}}$  term at  $x = (0.5, 0.5)$  over time.

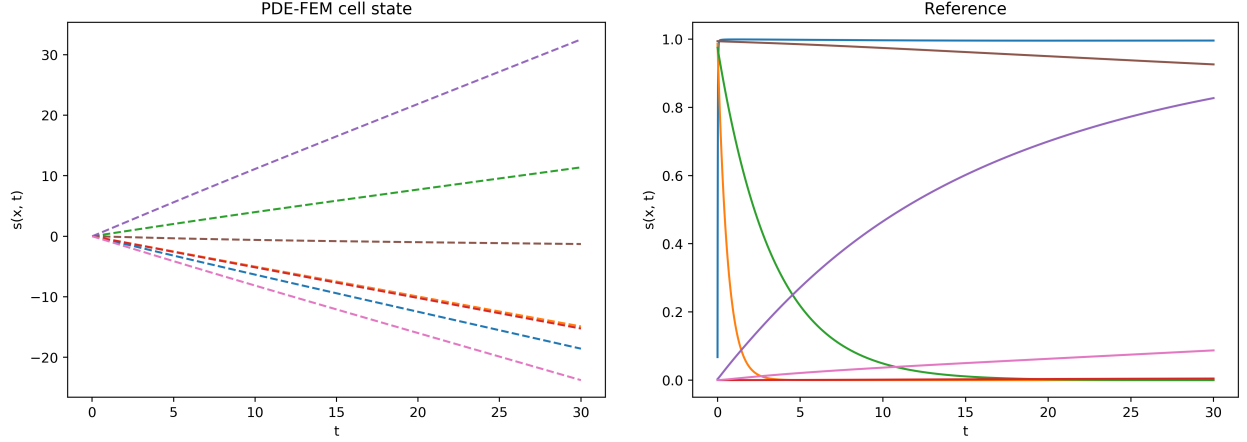


Figure 16: The hidden cell states  $s$  in the trained hybrid FEM-NN model (left) and the Beeler-Reuter model (right) at the spatial point  $x = (0.5, 0.5)$ .

We also inspect the predicted hidden cell states for  $s$  when there is no external stimulus, and compare to the true  $s$  from the Beeler-Reuter model. The values of these hidden states at spatial coordinate  $x = (0.5, 0.5)$  are plotted in fig. 16. The predicted cell states seem to grow almost linearly whereas the true cardiac cell model states range between 0 and 1. This indicates that the predicted cell states act as some form of time tracking, explaining why the slope after an external stimulus is very similar to the one from the training data.

In order to eliminate this source of overfitting, one could try to initialise the hidden cell states in a systematic way, and train for different initialisations of  $s$ . This could, for example, be achieved using the technique proposed in [38] in which a neural network is used to estimate an initial hidden cell state based on past observations of the transmembrane potential.

#### 4. Conclusion

In this paper, we demonstrated hybrid FEM-NN models, in which we augment PDEs with NN using FEM solvers. We demonstrate that the methodology of combining a traditional PDE solver in FEM with neural networks performs better than plain PINNs at solving the considered inverse problem for the heat equation when the unknown diffusion coefficient was discontinuous. The results suggest that strongly enforcing the PDE through a PDE solver improves the convergence of the optimisation. However, this technique comes with other new challenges in that the nonlinear and linear subproblems arising from the FEM-NN discretisation must remain solvable throughout training and well-established PDE solver tools are not optimised for large batch training or repeated evaluations on GPU. Additionally, the variational formulation used in the FEM requires integration of NN, for which efficient quadrature rules are currently unknown.

We also demonstrated the recovery of an unknown advection term in the advection-diffusion equation, including that the approximated advection velocity matches well with the true velocity. However, the learned advection term is relatively simple given that the gradient of the solution is supplied. Applying hybrid FEM-NN models to learn advection or other physical terms for a highly nonlinear problem is an interesting avenue for future work.

Furthermore, all neural networks shown have been relatively small, and finding optimal designs of the neural networks have not been part of our work. While all the tested NN are global functions mapping each point separately, avoiding the discretisation to be designed into the network, this also comes with a limitation with regards to learning differential operators. Because the network will only have local information for its input functions, it cannot produce differential terms without derivatives being explicitly supplied. Therefore, investigating the capabilities of a local NN defined on stencils, possibly designed as a convolutional NN as in [10], is an interesting pathway forward.

Finally, we have observed that the trained NN will attempt to compensate and produce a more accurate estimate without discretisation when during the training the discretisation error is high (the results are not included in the paper). In addition, even if the discretisation scheme is unstable in the ground truth model, the NN seems to be able to produce outputs that give reasonable solutions. The observation poses an interesting question for future work, namely: Is it possible to train a NN to alleviate discretisation errors and instabilities in such a way that it generalizes?

## 5. Acknowledgments

This work was supported by the Research Council of Norway through the FRINATEK program, project numbers 303362. Sebastian Mitusch was supported by the Norwegian Ministry of Education and Research. Miroslav Kuchta acknowledges support from the Research Council of Norway grant no. 280709.

## References

- [1] G. Marcus, Deep learning: A critical appraisal, arXiv preprint arXiv:1801.00631.
- [2] Z. Long, Y. Lu, B. Dong, PDE-Net 2.0: Learning PDEs from data with a numeric-symbolic hybrid deep network, *Journal of Computational Physics* 399 (2019) 108925. doi:10.1016/j.jcp.2019.108925.
- [3] Z. Long, Y. Lu, X. Ma, B. Dong, PDE-Net: Learning PDEs from data, in: *International Conference on Machine Learning*, PMLR, 2018, pp. 3208–3216.
- [4] L. Ruthotto, E. Haber, Deep neural networks motivated by partial differential equations, *Journal of Mathematical Imaging and Vision* (2019) 1–13doi:10.1007/s10851-019-00903-1.

- [5] M. Raissi, P. Perdikaris, G. E. Karniadakis, Physics-informed neural networks: A deep learning framework for solving forward and inverse problems involving nonlinear partial differential equations, *Journal of Computational Physics* 378 (2019) 686–707. doi:10.1016/j.jcp.2018.10.045.
- [6] A. M. Tartakovsky, C. O. Marrero, P. Perdikaris, G. D. Tartakovsky, D. Barajas-Solano, Learning parameters and constitutive relationships with physics informed deep neural networks, arXiv preprint arXiv:1808.03398.
- [7] M. Raissi, Deep Hidden Physics Models: Deep Learning of Nonlinear Partial Differential Equations, *Journal of Machine Learning Research* 19 (25) (2018) 1–24.
- [8] Y. Shin, J. Darbon, G. E. Karniadakis, On the convergence and generalization of physics informed neural networks, arXiv preprint arXiv:2004.01806.
- [9] J. Berg, K. Nyström, Neural network augmented inverse problems for PDEs, arXiv:1712.09685.
- [10] C. Rackauckas, Y. Ma, J. Martensen, C. Warner, K. Zubov, R. Supekar, D. Skinner, A. Ramadhan, Universal Differential Equations for Scientific Machine Learning, arXiv:2001.04385.
- [11] D. Z. Huang, K. Xu, C. Farhat, E. Darve, Learning Constitutive Relations from Indirect Observations Using Deep Neural Networks, *Journal of Computational Physics* 416 (2020) 109491. doi:10.1016/j.jcp.2020.109491.
- [12] T. Fan, K. Xu, J. Pathak, E. Darve, Solving Inverse Problems in Steady State Navier-Stokes Equations using Deep Neural Networks, arXiv:2008.13074.
- [13] A. Logg, G. N. Wells, DOLFIN: Automated finite element computing, *ACM Transactions on Mathematical Software (TOMS)* 37 (2) (2010) 20:1–20:28. doi:10.1145/1731022.1731030.
- [14] A. Paszke, S. Gross, F. Massa, A. Lerer, J. Bradbury, G. Chanan, T. Killeen, Z. Lin, N. Gimelshein, L. Antiga, A. Desmaison, A. Kopf, E. Yang, Z. DeVito, M. Raison, A. Tejani, S. Chilamkurthy, B. Steiner, L. Fang, J. Bai, S. Chintala, Pytorch: An imperative style, high-performance deep learning library, in: *Advances in Neural Information Processing Systems 32*, Curran Associates, Inc., 2019, pp. 8024–8035.
- [15] E. Haber, L. Ruthotto, E. Holtham, S.-H. Jun, Learning across scales—multiscale methods for convolution neural networks, in: *Thirty-Second AAAI Conference on Artificial Intelligence*, 2018.
- [16] R. T. Q. Chen, Y. Rubanova, J. Bettencourt, D. Duvenaud, Neural ordinary differential equations, in: *Proceedings of the 32nd International Conference on Neural Information Processing Systems, NIPS’18*, 2018, p. 6572–6583.

- [17] R. Glowinski, Finite element methods for incompressible viscous flow, in: Numerical Methods for Fluids (Part 3), Vol. 9 of Handbook of Numerical Analysis, Elsevier, 2003, pp. 3 – 1176. doi:10.1016/S1570-8659(03)09003-3.
- [18] E. Kharazmi, Z. Zhang, G. E. Karniadakis, Variational Physics-Informed Neural Networks For Solving Partial Differential Equations, arXiv:1912.00873.
- [19] U. Naumann, The Art of Differentiating Computer Programs: An Introduction to Algorithmic Differentiation, Society for Industrial and Applied Mathematics, Philadelphia, PA, USA, 2012.
- [20] S. Ulbrich, Analytical Background and Optimality Theory, Springer Netherlands, Dordrecht, 2009, pp. 1–95. doi:10.1007/978-1-4020-8839-1\_1.
- [21] M. S. Alnæs, A. Logg, K. B. Ølgaard, M. E. Rognes, G. N. Wells, Unified Form Language: A Domain-specific Language for Weak Formulations of Partial Differential Equations, ACM Trans. Math. Softw. 40 (2) (2014) 9:1–9:37. doi:10.1145/2566630.
- [22] S. K. Mitusch, S. W. Funke, J. S. Dokken, dolfin-adjoint 2018.1: automated adjoints for FEniCS and Firedrake, Journal of Open Source Software 4 (38) (2019) 1292. doi:10.21105/joss.01292.
- [23] R. Löhner, H. Antil, Revisiting Calderon’s Problem, arXiv:1912.02970.
- [24] L. M. Valnes, S. K. Mitusch, G. Ringstad, P. K. Eide, S. W. Funke, K.-A. Mardal, Apparent diffusion coefficient estimates based on 24 hours tracer movement support glymphatic transport in human cerebral cortex, Scientific Reports 10 (1) (2020) 1–12.
- [25] A. Kværnø, Singly Diagonally Implicit Runge–Kutta Methods with an Explicit First Stage, BIT Numerical Mathematics 44 (3) (2004) 489–502. doi:10.1023/B:BITN.0000046811.70614.38.
- [26] K. E. Skare, Gryphon-a module for time integration of partial differential equations in fenics, Master’s thesis, Institutt for matematiske fag (2012).
- [27] S.-Y. Shen, A numerical study of inverse heat conduction problems, Computers & Mathematics with applications 38 (7-8) (1999) 173–188. doi:10.1016/S0898-1221(99)00248-5.
- [28] A. D. Jagtap, E. Kharazmi, G. E. Karniadakis, Conservative physics-informed neural networks on discrete domains for conservation laws: Applications to forward and inverse problems, Computer Methods in Applied Mechanics and Engineering 365 (2020) 113028. doi:10.1016/j.cma.2020.113028.
- [29] A. D. Jagtap, G. E. Karniadakis, Extended Physics-Informed Neural Networks (XPINNs): A Generalized Space-Time Domain Decomposition Based Deep Learning Framework for Nonlinear Partial Dif-

- ferential Equations, *Communications in Computational Physics* (2020) 2002–2041 doi:10.4208/cicp.OA-2020-0164.
- [30] S. Wang, Y. Teng, P. Perdikaris, Understanding and mitigating gradient pathologies in physics-informed neural networks, arXiv preprint arXiv:2001.04536.
  - [31] A. D. Jagtap, K. Kawaguchi, G. E. Karniadakis, Adaptive activation functions accelerate convergence in deep and physics-informed neural networks, *Journal of Computational Physics* 404 (2020) 109136. doi:10.1016/j.jcp.2019.109136.
  - [32] C. Zhu, R. H. Byrd, P. Lu, J. Nocedal, Algorithm 778: L-BFGS-B: Fortran Subroutines for Large-Scale Bound-Constrained Optimization, *ACM Trans. Math. Softw.* 23 (4) (1997) 550–560. doi:10.1145/279232.279236.
  - [33] P. Virtanen, R. Gommers, T. E. Oliphant, M. Haberland, T. Reddy, D. Cournapeau, E. Burovski, P. Peterson, W. Weckesser, J. Bright, S. J. van der Walt, M. Brett, J. Wilson, K. J. Millman, N. Mayorov, A. R. J. Nelson, E. Jones, R. Kern, E. Larson, C. J. Carey, Í. Polat, Y. Feng, E. W. Moore, J. VanderPlas, D. Laxalde, J. Perktold, R. Cimrman, I. Henriksen, E. A. Quintero, C. R. Harris, A. M. Archibald, A. H. Ribeiro, F. Pedregosa, P. van Mulbregt, SciPy 1.0 Contributors, SciPy 1.0: Fundamental Algorithms for Scientific Computing in Python, *Nature Methods* 17 (2020) 261–272. doi:10.1038/s41592-019-0686-2.
  - [34] J. Sundnes, G. Lines, X. Cai, B. Nielsen, K. Mardal, A. Tveito, Computing the Electrical Activity in the Heart, *Monographs in Computational Science and Engineering*, Springer Berlin Heidelberg, 2007. doi:10.1007/3-540-33437-8.
  - [35] P. E. Farrell, J. E. Hake, S. W. Funke, M. E. Rognes, Automated adjoints of coupled PDE-ODE systems, *SIAM Journal on Scientific Computing* 41 (3) (2019) C219–C244. doi:10.1137/17M1144532.
  - [36] G. W. Beeler, H. Reuter, Reconstruction of the action potential of ventricular myocardial fibres, *The Journal of Physiology* 268 (1) (1977) 177–210. doi:10.1113/jphysiol.1977.sp011853.
  - [37] I. Ayed, E. de Bézenac, A. Pajot, J. Brajard, P. Gallinari, Learning Dynamical Systems from Partial Observations, arXiv:1902.11136.
  - [38] I. Ayed, N. Cedilnik, P. Gallinari, M. Sermesant, EP-Net: Learning Cardiac Electrophysiology Models for Physiology-based Constraints in Data-Driven Predictions, in: *FIMH 2019 - 10th International Conference on Functional Imaging of the Heart*, Springer, Bordeaux, France, 2019, pp. 55–63.